

Water Oxidation Catalysis using Amorphous Manganese Oxides, Octahedral Molecular Sieves (OMS-2), and Octahedral Layered (OL-1) Manganese Oxide Structures

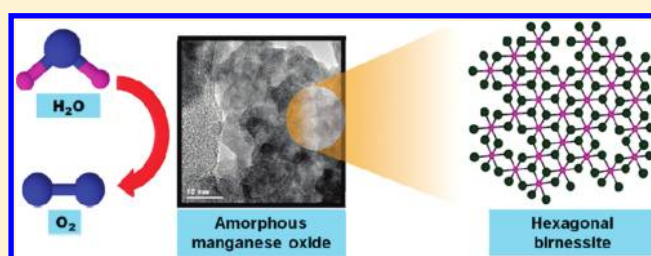
Aparna Iyer,[†] Joselyn Del-Pilar,[§] Cecil K. King'ondou,[†] Edward Kissel,[†] Hector F. Garces,[‡] Hui Huang,[†] Abdelhamid M. El-Sawy,[†] Prabir K. Dutta,^{*,§} and Steven L. Suib^{*,†,‡}

[†]Department of Chemistry and [‡]Institute of Materials Science, University of Connecticut, Storrs, Connecticut 06269, United States

[§]Department of Chemistry, Newman & Wolfrom Lab, 100 West 18th Avenue, The Ohio State University, Columbus, Ohio 43210, United States

Supporting Information

ABSTRACT: Water oxidation is the bottleneck in artificial photosynthetic systems that aim to split water into hydrogen and oxygen. However, water oxidation occurs readily in plants, catalyzed by the $\text{Mn}_4\text{O}_4\text{Ca}$ manganese cluster. In addition to this, manganese minerals are ubiquitous in nature displaying layered and tunnel structures. In this study, mixed valent porous amorphous manganese oxides (AMO), along with cryptomelane type tunnel manganese oxides (OMS-2) and layered birnessite (OL-1) have been used as water oxidation catalysts. Significantly higher turnovers were obtained with AMO (290 mmol O_2 /mol Mn) compared to tunnel structure OMS-2 (110 mmol O_2 /mol Mn) and layered structure OL-1 (27 mmol O_2 /mol Mn) in water oxidation tests with Ce^{4+} . Oxygen evolution was also confirmed under photochemical conditions using $\text{Ru}(\text{bpy})_3^{2+}$ as a photosensitizer and persulfate as a sacrificial agent. The differences in catalytic activity among these catalysts have been probed using X-ray diffraction, transmission electron microscopy, Raman and Fourier transform infrared (FTIR) spectroscopy, average oxidation state, and compositional analyses. Comparison of AMO against prominent manganese catalysts described in literature shows AMO provided the highest turnover numbers. AMO catalyst was also reusable after regeneration. O-18 labeling studies proved that water was the source of dioxygen and IR proved the structural stability of AMO after reaction. AMO is related to hexagonal birnessites such as layered biogenic manganese oxides or H^+ -birnessite that have cation vacancies in the MnO_2 sheets rather than completely filled $\text{Mn}^{3+}/\text{Mn}^{4+}$ sheets, and this is influential in catalytic activity.



INTRODUCTION

Total energy consumption in the world is projected to increase by 50% from 2009 to 2035.¹ More than 80% of today's energy is supplied by burning of fossil fuels: coal, natural gas, and petroleum.² In addition to increasing dependence on finite fossil fuel resources, rise in global atmospheric CO_2 levels caused by energy related burning of hydrocarbons is a major concern.³ Carbon dioxide emissions in the United States increased 3.9% in 2010, which is the highest yearly rise in CO_2 levels since 1988.⁴ A combination of such economic and environmental factors has created an urgent need for the development of alternative sources of energy that are clean and sustainable.

Hydrogen from solar water splitting is desired as a clean renewable energy source (eq 1).^{3,5} In the water splitting reaction however, the oxidation reaction involving multi-electron transfer is more difficult due to thermodynamic and kinetic limitations (eq 2).^{5,6} Hence, the focus is on catalysts to drive the water oxidation reaction (eq 2).^{7,8} High turnovers (of the order of 10^3) are achieved in eq 2 using oxides of ruthenium and iridium.^{9–13} However, the low natural abundances and high

costs render elements like ruthenium and iridium unsuitable for large scale water oxidation applications.

Photosynthesis in plants is a model process for generating chemical energy that utilizes sunlight and water.¹⁴ The $\text{Mn}_4\text{O}_4\text{Ca}$ manganese cluster in the core of Photosystem II (PS-II) catalyzes the four electron water oxidation process in plants.¹⁴ Efforts are being made to develop manganese catalysts mimicking the function of the PS-II core for artificial water oxidation.^{15–18}



Interest in manganese catalysts is also fueled by its biogeochemical presence and abundance.¹⁹ In nature, bacterial

Received: December 14, 2011

Revised: February 14, 2012

Published: February 21, 2012

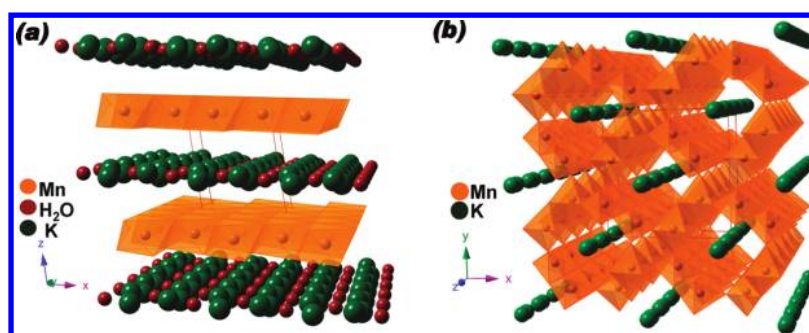


Figure 1. Representative structures of (a) octahedral layered manganese oxide OL-1 (birnessite) and (b) octahedral molecular sieves (OMS-2) having a 2×2 tunnel (cryptomelane).

and fungal strains oxidize Mn(II) to Mn(IV) oxides.^{20,21} For example, phyllophanes, such as vernadite, possess significant metal sorption capacities, and are formed by the action of *Pseudomonas putida* bacteria.^{21,22} Biogenic manganese species also play a key role in the sequestration of heavy metals from soil, phosphate adsorption from waters, oxidation–reduction, and cation–exchange reactions.^{19,20} Several biogenic transformations result in manganese oxides that are mixed phase, poorly crystalline, highly disordered, and compositionally diverse.¹⁹ A variety of manganese crystal structures such as layered, tunnel structures and spinels are found as ocean and freshwater nodules, coatings on rock surfaces, hydrothermal veins, and dendrites.¹⁹

Potassium containing manganese oxide octahedral molecular sieves (OMS-2) are synthetic analogs of naturally occurring tunnel-type manganese oxide mineral, cryptomelane. OMS-2 consists of MnO₆ octahedra forming 2×2 tunnels of $\sim 4.7 \text{ \AA} \times 4.7 \text{ \AA}$ size (Figure 1).²³ The 2×2 tunnels are formed by edge sharing and corner sharing of MnO₆ octahedra. The chemical composition of OMS-2 is $\text{KMn}^{4+}_7\text{Mn}^{3+}\text{O}_{16} \cdot n\text{H}_2\text{O}$ with K⁺ cations and H₂O molecules residing in the tunnel site.²⁴ Extensive catalytic studies have shown that OMS-2 is an excellent oxidation catalyst under thermal and photochemical conditions.^{25–27}

Octahedral layered materials (OL-1 or K-OL-1) are analogs of mineral birnessite formed by edge-sharing MnO₆ octahedra resulting in layers or sheets (Figure 1). They contain K⁺ ions and water molecules in the interlayers. Typically, layer spacings for OL-1 are on the order of 7 Å. OL-type materials are important in batteries,^{24,28} adsorbents,²⁸ environmental remediation,²⁸ and as intermediates in the formation of tunnel manganese oxides.^{29,30}

In addition to their active role in catalysis in nature, layered and tunnel-type manganese oxides contain Mn₄O₄ structural motifs. The Mn₄O₄ units can conform to various geometries resembling the Mn₄O₄Ca cluster in PS-II.^{31,32} Manganese is mixed valent in these materials and has the ability to cycle between +3 and +4 oxidation states during catalysis. These factors are crucial in mimicking the function of the Mn₄O₄Ca complex in PS-II.³³ This has inspired our interest in studying synthetic layered and tunnel structures of manganese oxides for water oxidation.

Besides the above-mentioned crystalline forms, amorphous manganese oxides (AMO) were first developed by our group as outstanding heterogeneous photocatalysts for 2-propanol oxidation.³⁴ Excellent selectivities were achieved in this reaction. The high activity observed in these materials has been linked to the ease of lattice oxygen mobility in the bulk

structure and excess surface oxygen.^{30,34} Since then, several studies by our group have exemplified the use of amorphous manganese oxides for photo-oxidation of highly toxic compounds such as halogenated hydrocarbons, organophosphates, and *n*-nitrosodimethylamine.^{35–37} Recent work has shown that AMO is a good catalyst for thermocatalytic CO oxidation.³⁸ Despite the wide variety of catalytic studies, the understanding of amorphous manganese oxide as a catalyst is far from complete.

In this study, AMOs along with tunnel structured and layered manganese oxides such as OMS-2 (cryptomelane) and OL-1 (birnessite) are examined in detail as water splitting catalysts in chemical ($\text{Ce}^{4+}/\text{Ce}^{3+}$ ($E^\circ = +1.7 \text{ V}$)) and photochemical ($\text{Ru}(\text{bpy})_3^{3+}/\text{Ru}(\text{bpy})_3^{2+}$ ($E^\circ = +1.24 \text{ V}$)) systems. Water oxidation tests were carried out with oxidizing agents such as cerium ammonium nitrate (CAN) or $\text{Ru}(\text{bpy})_3^{3+}$ that are representative of the $4 \times 1 \text{ e}^-$ process occurring during photosynthesis.^{12,39} Structural (X-ray diffraction (XRD), transmission electron microscopy (TEM), Fourier transform infrared (FTIR), Raman spectroscopy) and compositional (inductively coupled plasma-atomic emission spectroscopy (ICP-AES), average oxidation state (AOS), thermogravimetric analysis (TGA), energy dispersive X-ray (EDX) spectroscopy) characterization of catalysts have been used to understand differences among these materials and their effects on catalytic activity.

EXPERIMENTAL METHODS

Synthesis Procedures. *AMO.* AMO was prepared at room temperature by the reduction of KMnO_4 with oxalic acid.³⁴ Specifically, 1.58 g of KMnO_4 was dissolved in 60 mL of distilled deionized water (DDW), and 2.28 g of oxalic acid was dissolved in 100 mL of DDW. The potassium permanganate solution was then added dropwise to the oxalic acid solution. The resulting reaction mixture was kept stirring for 2 h at room temperature. The brown slurry was filtered, and the product obtained was washed several times with deionized water and dried at 90 °C overnight.

OMS-2. A solid-state reaction was used to prepare OMS-2.⁴⁰ In this synthesis, Mn^{2+} was reacted with Mn^{7+} in the ratio of 2:3. Typically, 9 mmol of $\text{Mn}(\text{Ac})_2 \cdot 4\text{H}_2\text{O}$ and 6 mmol of KMnO_4 were ground homogeneously in an agate mortar for 20 min. The mixture was transferred to a capped vial and maintained in an oven at 120 °C for 4 h. The resulting powder was washed with deionized water several times and then dried at 80 °C overnight.

OL-1. Octahedral layered material (birnessite) containing potassium was synthesized according to a procedure reported

by Gao et al.⁴¹ In a typical synthesis an aqueous solution A of 200 mL volume containing 92 mL of ethanol and 33.6 g of potassium hydroxide was prepared. Another aqueous solution B of 150 mL volume containing 9.48 g of potassium permanganate was prepared. Solution A was slowly added to solution B under vigorous stirring. The resulting mixture was stirred for 1 h and aged at 80 °C for 48 h. The product was washed several times with DDW until a pH of less than 9 was attained. The washed sample was dried overnight at 80 °C.

Catalyst Characterization. XRD data were obtained on a Scintag-2000 PDS diffractometer with Cu K α (1.54 Å) radiation. The beam voltage and beam current were set to 45 kV and 40 mA, respectively. Continuous scans were taken in a 2 θ range of 5–80° with a scan rate of 0.02 deg/s. Peaks were indexed using the Joint Committee on Powder Diffraction Society (JCPDS) database. The morphologies of the manganese oxide materials were studied using TEM on a JEOL JEM-2010 FasTEM operating at 200 kV. The samples for TEM were prepared by dispersing the powders in ethanol followed by sonication for 5 min. The suspension was then dropped on a carbon coated copper grid.

Raman measurements were performed at room temperature on a Renishaw 2000 Ramascope. A cooled charge-coupled device (CCD) detector was used to collect the scattered light dispersed by an 1800 lines/mm grating. An Ar⁺ laser (514.4 nm) was used as the excitation source. The laser power was set to 10 mW to prevent sample denaturation. The spectrometer was calibrated with a silicon wafer prior to sample measurements. FTIR spectra were obtained using a Nicolet 8700 FTIR spectrometer with a resolution of 4 cm⁻¹. Infrared data (600 through 350 cm⁻¹) were collected using a DTGS detector with a polyethylene window. Samples were prepared by diluting with cesium iodide in a ratio of 1:100 and pressed into pellets. The spectral background was collected using pure CsI discs.

Manganese and potassium contents in the samples were determined using ICP-AES on a Thermo Jarrell Ash ICAP 61E Trace Analyzer. Manganese oxide samples weighing approximately 10 mg were digested in 5 mL of concentrated HCl (36.5%) in Erlenmeyer flasks. The flasks were kept at 70 °C until clear solutions were obtained. The digested samples were diluted to an estimated concentration. Manganese and potassium standards (0–25 ppm) were prepared for calibration. The samples and standards were then analyzed by ICP-AES. Surface elemental ratios were measured using EDX spectroscopy. Measurements were performed on an Amray model 1810D instrument operated at 20.0 kV. EDX spectra were acquired and processed with an Amray model PV 9800 EDS system. The energy resolution of the instrument was 149 eV (Full width of half-maximum) for the 5.89 keV Mn K α line.

Potentiometric titrations were used to measure the average oxidation state (AOS) of manganese oxide samples. The samples were dissolved in HCl to convert all the manganese to Mn²⁺ and titrated to a Mn³⁺ complex with sodium pyrophosphate versus potassium permanganate. This gives total Mn content, based on which the AOS is determined by reducing the solid to Mn²⁺ using ferrous ammonium sulfate and back-titrating the excess Fe²⁺ with a permanganate standard.

TGA in air was performed on a Hi-Res TGA 2950 thermogravimetric analyzer. The air flow rate was set at 60 mL/min, and samples were heated from room temperature to 700 °C. Brunauer–Emmett–Teller (BET) surface area measurements were done on a Quantachrome Autosorb iQ2

instrument. All samples were degassed before analysis at 100 °C for 6 h to remove any physically adsorbed species.

Water Oxidation Test with O₂ Detection Done Using a Clarke-Type Electrode. Chemical water oxidation tests were conducted in 80-mL aqueous solutions containing 0.25 M cerium ammonium nitrate (CAN).¹⁶ In an airtight system, a quartz reaction vessel containing 35 mg of catalyst suspended in water was purged with argon for two hours to remove all dissolved oxygen. A solution containing CAN was deoxygenated separately. The CAN solution was injected into the quartz reaction vessel taking caution not to introduce atmospheric oxygen into the system.¹⁶ Dissolved oxygen in the reaction vessel was measured at room temperature using a Clarke-type oxygen electrode (YSI 550A Yellow Springs Instrument, OH) containing a silver anode, a gold cathode, and a temperature sensor.

Photochemical water oxidation tests were conducted in a quartz reaction vessel containing 35 mg of catalyst, 1.5 mM Ru(bpy)₃²⁺, 13 mM Na₂S₂O₈, and 68 mM Na₂SO₄ in 80 mL buffered aqueous solutions (pH 5–6).⁷ The buffer solution was made up of Na₂SiF₆–NaHCO₃. Reactants in the quartz vessel were sonicated for 30 min and purged with argon for two hours to remove all dissolved oxygen from the aqueous solution. The quartz vessel was irradiated with a continuous output xenon lamp set at 250-W power. An IR filter and a bandpass filter ($\lambda = 450 \text{ nm} \pm 20 \text{ nm}$) were placed in between the quartz vessel and the light source. During the course of reaction, the quartz vessel was kept at room temperature by cooling in a water bath. Dissolved oxygen in the reaction vessel was measured at room temperature using a Clarke-type oxygen electrode (YSI 550A Yellow Springs Instrument, OH) equipped with a temperature sensor.

Water Oxidation Tests with O₂ Detection Done Using Gas Chromatography. Chemical water oxidation tests with 0.25 M CAN and 35 mg of catalyst were done in 40 mL aqueous solutions. For photochemical water oxidation, a photolysis vessel containing Ru(bpy)₃²⁺ (4 mg), Na₂S₂O₈ (200 mg), Na₂SO₄ (600 mg), and 35 mg of catalyst in 40 mL of buffered (Na₂SiF₆–NaHCO₃ buffer) aqueous solution was used. After purging with nitrogen, the vessel was illuminated with a xenon lamp. For both cases, about 50 μ L of gas sample drawn from the headspace was injected into a SRI 310 gas chromatograph equipped with a thermal conductivity detector (TCD) and a 13 \times packed molecular sieve column. The helium carrier gas flow rate was set at 20 mL/min at 40 psi. The column and TCD temperatures were 80 and 100 °C respectively with a hold time of 1 min.

Water Oxidation Test with H₂¹⁸O and Mass Spectrometric Detection. Water oxidation test with 10 at % ¹⁸O-labeled water (Sigma Aldrich) were done in 5-mL solutions containing 3 mg catalyst and 0.02 M CAN. A vial containing 3 mg of AMO catalyst in 2.5 mL water was sealed and purged with nitrogen gas for 10 min. Another vial containing 2.5 mL CAN solution was also purged with nitrogen gas. The CAN solution was injected into the catalyst suspension. The system was kept airtight. About 1000 μ L of gas sample from the headspace was injected into the mass spectrometer. Oxygen was detected using a Cirrus Residual Gas Analyzer (MKS Spectra Products) mass spectrometer equipped with a dual Faraday and multiplier detector. The values of m/z 36 (¹⁸O¹⁸O), m/z 34 (¹⁶O¹⁸O), and m/z 32 (¹⁶O¹⁶O) were monitored. By use of the same procedure described above, control experiments were conducted with unlabeled water.

Analysis of Dissolved Mn Content in Reactant Solutions. Atomic absorption spectroscopy (AAS) was used to detect Mn ions in reactant solutions. Water oxidation tests were carried out for 30 min in 80-mL aqueous solutions containing 35 mg of catalyst and 0.25 M CAN. After 30 min, the catalysts were separated from reactant solutions by filtration. The solutions were then analyzed for Mn content using a Perkin-Elmer Atomic Absorption Spectrometer 3100. Samples for AAS were prepared by diluting 5–10 mL of the reactant solutions to 50 mL after the removal of catalysts by filtration.

RESULTS

Structure, Morphology, and Composition of Catalysts. XRD was used to identify phases and crystallinity of the as synthesized manganese oxide samples (Figure 2). The XRD

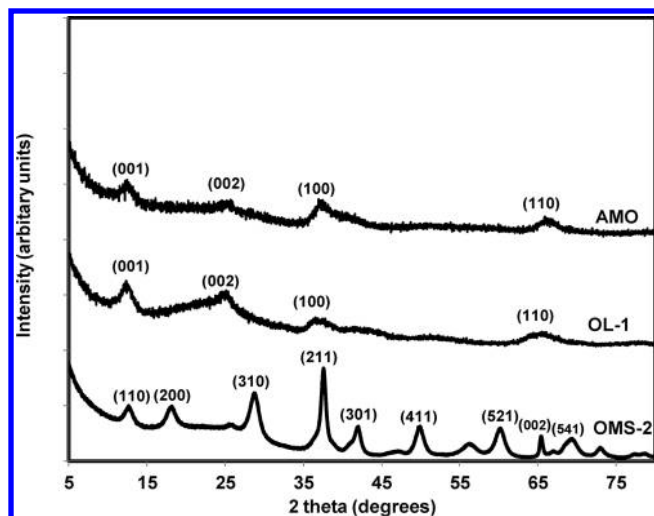


Figure 2. XRD patterns of AMO, OL-1, and OMS-2.

pattern obtained for AMO compares well with previous studies.³⁴ X-ray patterns of OMS-2 and OL-1 conform to the pure cryptomelane phase (JCPDS 29–1020) and K⁺-birnessite phase, respectively.^{42,43} In comparison with literature data, XRD patterns of OMS-2 and OL-1 show low peak intensities and peak broadening. This indicates low crystallinity of these samples. Amorphous manganese oxide contains three peaks of low intensity appearing at *d*-spacings 7.10 Å (12.46°), 2.41 Å (37.2°), and 1.41 Å (66.2°). A comparison of XRD patterns in Figure 2 shows that AMO is similar to turbostratic birnessite.

Morphology studies using TEM reveal that AMO consists of aggregates of nanoparticles (Figure 3a). A high-resolution TEM (HRTEM) image shows nanocrystallites of AMO with highly random orientation (Figure 3b) and crystallite sizes of less than 10 nm. The inset shows a selected area diffraction pattern (SAED) having diffuse rings or halos thus confirming the amorphous nature of the catalyst. OMS-2 has nanorod morphology as seen in the TEM image in Figure 3c. A typical HRTEM image of OMS-2 is shown in Figure 3d. The OMS-2 nanorods are 10–30 nm in width and 30–100 nm in length. OL-1 consists of nanoparticle aggregates as seen in the TEM image in Figure 3e. A HRTEM image of OL-1 shows a flakelike morphology with the size of each flake being 10–50 nm (Figure 3f).

Samples of AMO, OL-1, and OMS-2 were characterized using Raman and FTIR spectroscopy. Raman and FTIR spectroscopy are powerful tools to probe vibrational behavior

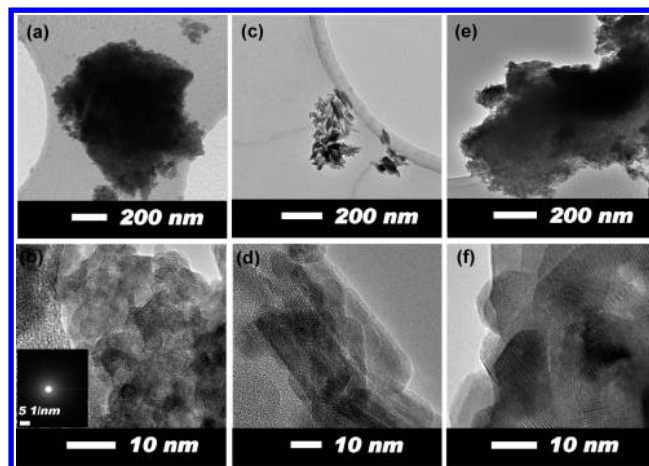


Figure 3. TEM images (top row): (a) AMO, (c) OMS-2, (e) OL-1. HRTEM images (bottom row): (b) AMO (inset SAED pattern), (d) OMS-2, (f) OL-1.

of lattices and hence probe structural differences and short-range order in amorphous or poorly crystalline phases of manganese oxides. Figure 4 presents Raman spectra of AMO,

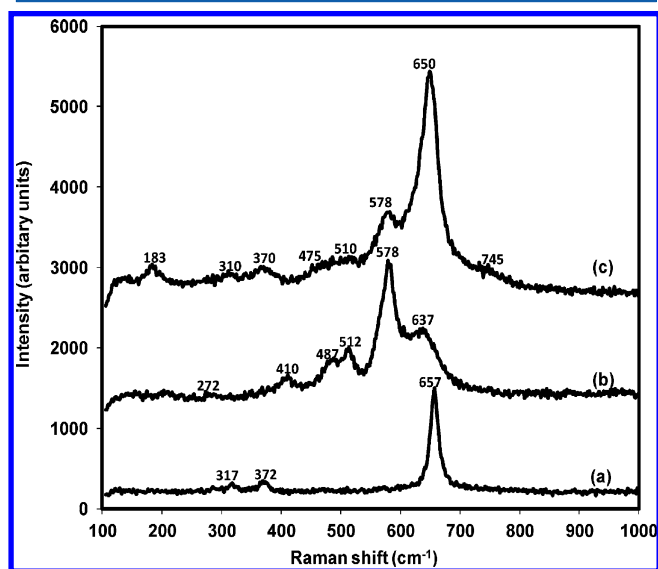


Figure 4. Raman spectra of (a) AMO, (b) OL-1, and (c) OMS-2 samples.

OL-1, and OMS-2. AMO has one strong band located at 657 cm⁻¹ (Figure 4a). OL-1 has Raman bands at 578 and 637 cm⁻¹ (Figure 4b). OMS-2 has two prominent Raman bands located at 578 and 650 cm⁻¹ (Figure 4c). The Raman band positions of OL-1 and OMS-2 are in good agreement with previous studies on cryptomelane and birnessite, respectively.^{44,45}

Metal–oxygen bonds are sensitive to infrared, and hence disordered components that cannot be identified by XRD can be elucidated by infrared analysis. FTIR data were collected for AMO, OL-1, and OMS-2 structures (Figure 5). In the Far-IR range, AMO exhibits two broad features at 519 and 437 cm⁻¹ (Figure 5a). OMS-2 exhibits one band of strong intensity at 527 cm⁻¹, other bands at 473 and 427 cm⁻¹, and a shoulder at 560 cm⁻¹ (Figure 5b). OL-1 exhibits three IR bands located at 516, 484, and 422 cm⁻¹ (Figure 5c). The location of the IR

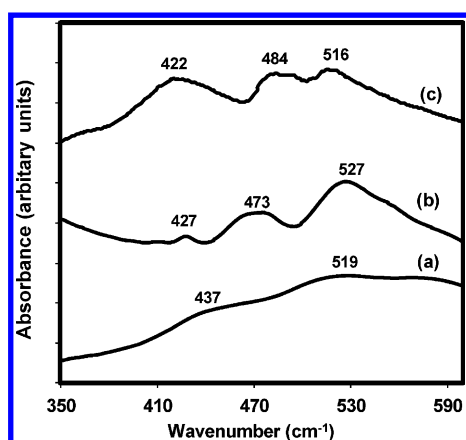


Figure 5. Infrared spectra of (a) AMO, (b) OMS-2, and (c) OL-1 samples.

bands for OMS-2 and OL-1 match with that of cryptomelane and birnessite reported previously.⁴⁶

Energy dispersive X-ray (EDX) spectroscopy was used to analyze surface potassium to manganese ratios in the manganese oxide catalysts. The potassium to manganese (K/Mn) atomic weight ratio in AMO (K/Mn = 0.01) was much lower than in OMS-2 (K/Mn = 0.11) or OL-1 (K/Mn = 0.18) (Table 1). The compositions of the catalysts were determined

Table 1. Composition and Surface Areas of Catalysts Used in This Study

catalyst	composition	K/Mn ratio by EDX	AOS	BET surface area m ² /g
AMO	K _{0.056} MnO _{1.98} ·0.45H ₂ O	0.01	3.91	184
OMS-2	K _{0.16} MnO _{1.97} ·0.14H ₂ O	0.11	3.79	140
OL-1	K _{0.5} MnO _{1.99} ·1.1H ₂ O	0.18	3.63	99

by combining ICP-AES data for manganese and potassium content, average oxidation states of manganese, and TGA data (Table 1). Water content was determined by weight loss in TGA seen around 160–180 °C (Figure S1, Supporting Information).

The average oxidation state of Mn in these samples varied (Table 1). In AMO, the average oxidation state of Mn is 3.91. AMO contains less than 10% Mn³⁺ ions in the structure. The OL-1 sample on the other hand, has a lower average oxidation state of 3.63 thus containing a much higher proportion of lower oxidation state species such as Mn³⁺. OMS-2 has an average manganese oxidation state of 3.79. Hence, among the three catalysts tested, OL-1 has the highest amount of potassium in the structure and lowest average Mn oxidation state.

Brunauer–Emmett–Teller (BET) measurements were used to determine surface areas of the samples. The surface areas of the three catalysts AMO, OMS-2, and OL-1 are 184, 140, and 99 m²/g, respectively (Table 1).

Water Oxidation Tests with AMO, OMS-2, and OL-1 Using CAN as an Oxidant. Water oxidation tests were conducted in 80-mL deoxygenated aqueous solutions containing manganese oxide catalysts and cerium ammonium nitrate (CAN) as a sacrificial electron acceptor. A Clarke-type O₂ electrode (YSI 550A Yellow Springs Instrument, OH) was used for detection of dissolved oxygen produced in these solutions. Figure 6 shows dissolved oxygen content in reactant solutions monitored for 30 min at room temperature. Among the

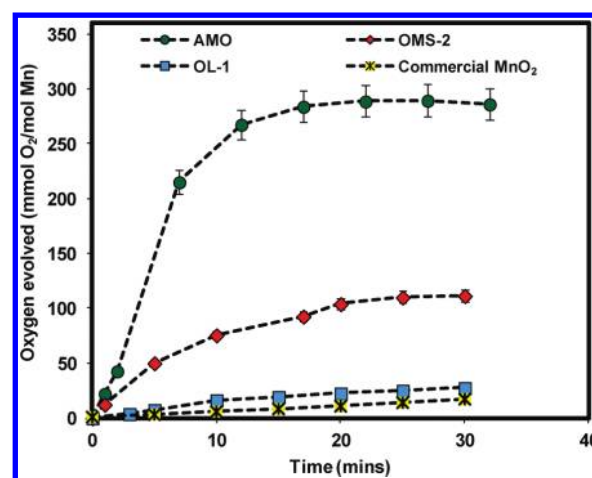


Figure 6. Dissolved oxygen measurements in aqueous solutions containing manganese oxide catalysts and 0.25 M cerium ammonium nitrate as an oxidant. Reactions were monitored for 30 min at room temperature, and a Clarke-type electrode was used for O₂ detection.

samples tested in this study, maximum oxygen evolution was observed when AMO was used as a catalyst with a turnover number of 290 mmol O₂/mol Mn. With OMS-2 catalyst, a turnover number of 110 mmol O₂/mol Mn was achieved. OL-1 gave a turnover of 27 mmol O₂/mol Mn. When commercial MnO₂ was tested in our system, a maximum turnover of 17 mmol O₂/mol Mn was obtained. Initial reaction rate for oxygen evolution using AMO was 20 times higher than the least active sample OL-1 (Table 2).

Table 2. Initial Rates of Dissolved Oxygen with AMO, OMS-2, and OL-1 Catalysts Tested under Chemical (CAN Oxidant) and Photochemical Conditions (Ru(bpy)₃²⁺ Oxidant)

catalyst	initial rate of O ₂ evolution (s ⁻¹)	
	CAN oxidation	Ru(bpy) ₃ ²⁺ photochemical oxidation
AMO	5.2 × 10 ⁻⁴	6.3 × 10 ⁻⁵
OMS-2	1.1 × 10 ⁻⁴	5.3 × 10 ⁻⁵
OL-1	2.8 × 10 ⁻⁵	4.7 × 10 ⁻⁶

Oxygen evolution in the CAN system was confirmed using gas chromatographic (GC) analyses of gaseous products collected in the headspace of the reaction mixture. In the case of the AMO catalyst, continuous oxygen evolution was observed for 60 min (Figure 7). In terms of total mol O₂/mol Mn, the catalytic activity followed the order: AMO > OMS-2 > OL-1. There is an excellent correlation between the catalytic activity trend observed for oxygen in the gas phase and the trend observed for dissolved oxygen measurements in the same systems (see Figure 7 and Figure 6). The total mol O₂/mol Mn in the headspace after 60 min from AMO exceeded that of the least active sample OL-1 by a factor of 30 (Figure 7).

Mass spectrometric measurements were carried out with ¹⁸O labeled water (10 atom % H₂¹⁸O), AMO catalyst, and CAN oxidant. The signals of 32, 34, and 36 m/z were monitored. The ³⁴O₂:³²O₂ ratio, obtained by averaging peak intensities for these two masses, was 0.21, which is close to the theoretically expected value of 0.22 (Figure S2, Supporting Information). The theoretical distribution of oxygen species from the ¹⁸O-labeled water was determined to be 81, 18, and 1% for ³²O₂,

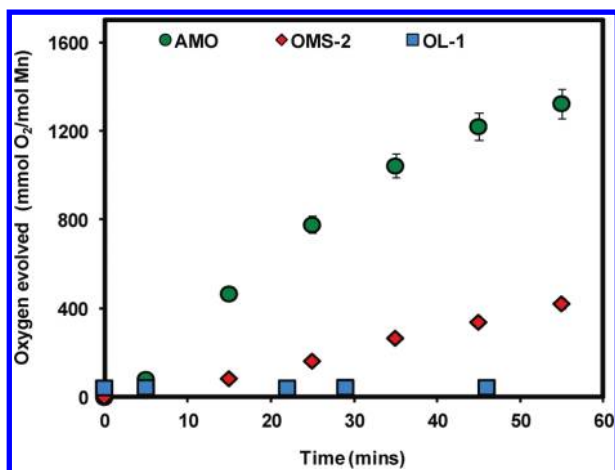


Figure 7. Gas chromatographic detection of oxygen evolved in the headspace of reactions containing manganese oxide catalysts and 0.25 M cerium ammonium nitrate.

$^{34}\text{O}_2$, and $^{36}\text{O}_2$, respectively. This experiment confirms that water was the source of dioxygen evolved in the gas phase. The difference seen in the actual versus theoretical ratios of $^{34}\text{O}_2$: $^{32}\text{O}_2$ intensities might be due to slight air leaks into the system. The same experiment was conducted with unlabeled water and the $^{34}\text{O}_2$: $^{32}\text{O}_2$ signal ratio was close to zero (Figure S2, Supporting Information).

Reusability Test with AMO and Characterization of AMO after Reaction with CAN. The reusability of the AMO catalyst was tested. After water oxidation test with 0.25 M CAN, the catalyst was separated from the reaction mixture by filtration. The catalyst was washed several times to remove any cerium ions that might have adsorbed on the surface and regenerated by drying at 90 °C overnight (designated as “regenerated catalyst”). To study the possibility of adsorption of cerium ions on the AMO catalyst after reaction, samples were collected after 1 wash cycle and 6 wash cycles during the washing process. EDX analyses of these samples showed that the average atomic weight percentage of cerium decreased from 4.8% after 1 wash cycle to 1.7% after 6 wash cycles (Table S1, Supporting Information). This indicates that the adsorbed cerium on the catalyst could be removed by the washing process.

The regenerated catalyst was then subjected to water oxidation tests using fresh CAN solution (0.25 M). As before, dissolved oxygen was measured in aqueous solution containing the catalyst and CAN. Measurements were conducted at room temperature using a Clarke-type electrode for O_2 detection. In this test, the regenerated AMO catalyst was reusable without loss of catalytic activity and gave equivalent turnover numbers as the fresh catalyst (Figure 8).

The regenerated AMO catalyst was also analyzed using FTIR spectroscopy to check for structural changes (parts a and b of Figure S3, Supporting Information). Comparison of IR spectra of fresh AMO and regenerated AMO revealed that AMO did not undergo any observable phase change after reaction. The BET surface area of the regenerated AMO catalyst was 160 m^2/g as opposed to the fresh catalyst, which had a BET surface area of 184 m^2/g . A decrease in BET surface area after reaction might be due to particle aggregation.

Characterization of Catalysts after Water Oxidation Reaction with CAN. XRD was performed on all catalysts (AMO, OMS-2, and OL-1) recovered after water oxidation

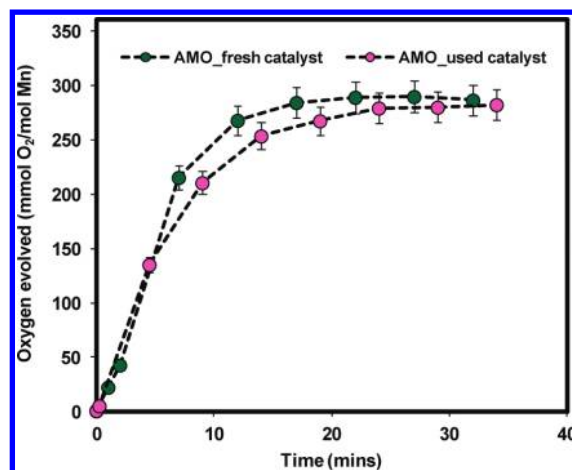


Figure 8. Reusability test for AMO catalyst: Dissolved oxygen measurements in aqueous solutions containing AMO-fresh catalyst and AMO-used catalyst. Reactions were carried out at room temperature for 30 min using 0.25 M cerium ammonium nitrate as an oxidant.

reaction with 0.25 M CAN to access structural changes (Figures S4 and S5, Supporting Information). There was no change seen in case of AMO (Figure S5, Supporting Information) and OMS-2 (Figure S4, Supporting Information) catalysts. In the case of OL-1, the intensity of the peaks of the recovered material was too low to determine if there was any change in the layering.

Dissolved Mn content in reactant solutions was monitored using AAS (Table S2, Supporting Information). The reactions were carried out in 80-mL aqueous solutions containing 0.25 M CAN. The filtrates were analyzed after reaction. In case of OMS-2 and OL-1, Mn ions were not detected in solution. In case of AMO, 0.9% of the total Mn in the catalyst was found in solution. However, the amount of O_2 obtained using AMO catalyst with CAN oxidant (Figure 6) far exceeded the amount of dissolved Mn in solution.

Water Oxidation Tests with AMO, OMS-2, and OL-1 Using Photochemical Reaction with $\text{Ru}(\text{bpy})_3^{2+}$. Activity of manganese oxides under photochemical oxidation conditions was tested in buffered aqueous solutions containing catalyst, $\text{Ru}(\text{bpy})_3^{2+}$, $\text{Na}_2\text{S}_2\text{O}_8$, Na_2SO_4 under visible light irradiation (Figure 9). Similar to water oxidation results in the CAN system, the dissolved oxygen content with AMO catalyst was the highest (84 $\text{mmol O}_2/\text{mol Mn}$) among the three manganese oxides tested (see Figure 6 for comparison). The total moles of oxygen evolved per mol Mn followed the order: AMO (84 $\text{mmol O}_2/\text{mol Mn}$) > OMS-2 (61 $\text{mmol O}_2/\text{mol Mn}$) > OL-1 (10 $\text{mmol O}_2/\text{mol Mn}$). Activity of AMO was 8 times higher than the least active sample OL-1. In contrast, experiments done with commercial MnO_2 gave 7 $\text{mmol O}_2/\text{mol Mn}$. Figure 9 also shows that, in the first 15 min of reaction, a higher oxygen evolution activity is observed with OMS-2 than with AMO. However, at 30 min of reaction time, the activity with AMO reaches a maximum turnover of 84 $\text{mmol O}_2/\text{mol Mn}$, whereas with OMS-2 the maximum turnover is 61 $\text{mmol O}_2/\text{mol Mn}$. In photochemical water oxidation with $\text{Ru}(\text{bpy})_3^{2+}$, initial reaction rates of oxygen evolution are a magnitude lower than reaction rates in chemical water oxidation with CAN (Table 2). However, a similar trend as seen in oxidation with CAN is observed here, where the initial rate of O_2 evolution

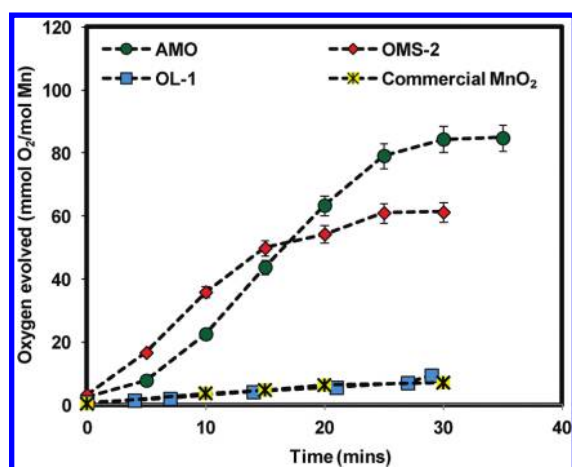


Figure 9. Dissolved oxygen measurements in aqueous solutions containing manganese oxide catalysts and $\text{Ru}(\text{bpy})_3^{2+}$ as an oxidant under photochemical conditions. Reactions were monitored for 30 min at room temperature and a Clarke-type electrode was used for O_2 detection.

using AMO catalyst is ~ 13 times higher than with OL-1 catalyst.

GC studies of gas samples collected from the headspace of the reaction mixtures confirmed the oxygen activity seen with the three manganese oxide catalysts (Figure 10). Here again,

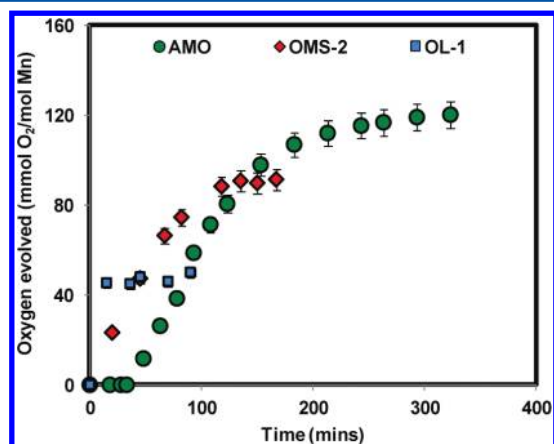


Figure 10. GC detection of oxygen evolved in the headspace of reactions containing manganese oxide catalysts and $\text{Ru}(\text{bpy})_3^{2+}$ during photochemical water oxidation.

AMO catalyst gave the maximum turnover followed by OMS-2 and OL-1. As seen with dissolved oxygen measurements in Figure 9, oxygen evolution from AMO begins after an induction period which is not the case with OMS-2. Continuous oxygen evolution was observed for 300 min in case of AMO catalyst (Figure 10). This is unique since amorphous calcium manganese oxides lose their activity during extended reaction times.¹⁶

Oxygen Evolution Activity of Manganese Oxides from Reported Literature. A direct comparison of turnover numbers among reported heterogeneous manganese oxides for water oxidation catalysis is difficult. Several reaction parameters such as the nature of the sacrificial oxidant, oxidant amount, reaction volumes, catalyst amount, and surface areas affect water oxidation results. Another variation among literature reports is the detection method used for measuring

the evolved oxygen gas. Turnover numbers and reaction rates are higher in systems using CAN as the sacrificial electron acceptor as opposed to those achieved in photochemical oxidation with $\text{Ru}(\text{bpy})_3^{2+}$ (Table 2).^{16,39}

In this study, we made valid comparisons by applying uniform reaction conditions for testing several heterogeneous manganese oxide catalysts reported in the literature. Procedures from literature references were followed as closely as possible for synthesizing catalysts for comparison.^{16–18,47,48} Catalysts have been synthesized under our laboratory conditions, hence deviations might occur. Nevertheless, this study provides a good measure of catalytic activities of various manganese oxide catalysts for oxygen evolution.

Water oxidation tests were conducted in 80-mL reaction volume containing the oxide catalyst and 0.1 M CAN as an oxidizing agent. Dissolved oxygen levels were monitored for 30 min using a Clarke-type oxygen electrode. Turnover numbers are reported as $\text{mmol O}_2/\text{mol Mn}$. The manganese amount for each catalyst was determined using ICP-AES. The oxygen evolution results are shown in Figure 11. A comparison of

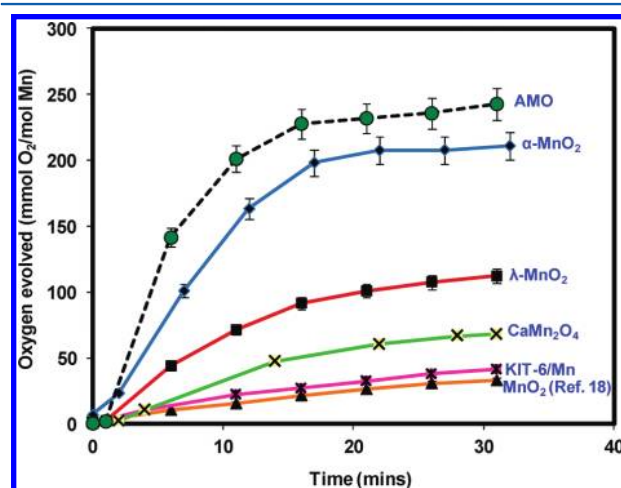


Figure 11. Oxygen evolution activity of AMO in comparison against manganese oxide catalysts reported in literature.

catalytic activities reveals that amorphous manganese oxide (AMO) catalyst gave a TON of 242 $\text{mmol O}_2/\text{mol Mn}$ compared to $\alpha\text{-MnO}_2$ -nanotubes (TON = 211), $\lambda\text{-MnO}_2$ -LT (TON = 112), CaMn_2O_4 (TON = 67), KIT-6/Mn-calcined at 600 °C (TON = 41), and MnO_2 (Shilov et al) (TON = 33). These turnover numbers are lower limit values, assuming every Mn atom is an active site.

DISCUSSION

This study highlights the use of amorphous manganese oxide as an efficient water oxidation catalyst compared to tunnel type manganese oxide OMS-2 (cryptomelane) and layered manganese oxide OL-1 (birnessite), both of which are extensively investigated materials.^{23,29} Among the manganese oxides tested in this work, AMO produced the highest moles of oxygen followed by OMS-2 and OL-1 under both chemical (with CAN) and photochemical oxidation (with $\text{Ru}(\text{bpy})_3^{2+}$) conditions.

Oxygen evolution activity displayed by the catalysts followed the trend $\text{AMO} > \text{OMS-2} > \text{OL-1}$ in chemical and photochemical water oxidation (see Figures 6, 7, 9, and 10 and Table 2). For example, the TONs obtained from dissolved

oxygen measurements with CAN are: AMO (290 mmol O₂/molMn) > OMS-2 (110 mmol O₂/mol Mn) > OL-1 (27 mmol O₂/mol Mn) (Figure 6). Initial rates of O₂ evolution in these reactions are $5.2 \times 10^{-4} \text{ s}^{-1}$ for AMO, followed by $1.1 \times 10^{-4} \text{ s}^{-1}$ for OMS-2, and $2.8 \times 10^{-5} \text{ s}^{-1}$ for OL-1 (Table 2). In both chemical and photochemical oxidation, the activity of AMO is a magnitude higher than that of the least active sample OL-1.

Interestingly, despite the structural resemblance from XRD between AMO and OL-1, the catalytic activity of AMO is markedly different (Figure 2). Tunnel structure OMS-2 performed better than OL-1, which is layered with an open MnO₆ framework. The discussion primarily focuses on the correlations between the catalytic activity trends and the compositional and structural differences manifested by these three manganese oxide catalysts, as elucidated by XRD, Raman and FTIR spectroscopy, BET measurements, Mn AOS, and composition experiments.

Structural Similarities and Differences between the Mn Oxides. From XRD, the patterns of both AMO and OL-1 resemble that of turbostratic birnessite⁴⁹ and are distinguished from regular K⁺-birnessite where the MnO₂ sheets are well oriented along the *c*-axis (Figure 2).^{43,49} Peaks appearing at $\sim 2.4 \text{ \AA}$ ($37^\circ 2\theta$) and $\sim 1.4 \text{ \AA}$ ($66^\circ 2\theta$) are *hk0* bands. These peaks are broad and asymmetric on the higher angle side indicating high turbostraticity in stacking. Peaks observed at $\sim 7 \text{ \AA}$ ($\sim 12^\circ 2\theta$) and $\sim 3.5 \text{ \AA}$ ($\sim 24^\circ 2\theta$) correspond to *00L* basal reflections. Broadening of the *00L* reflections and low intensities also indicate that stacking of the birnessite sheets in both samples are highly random.^{43,50} A small number of sheets are stacked, probably 2–3 sheets on average.²² Closer observation reveals that the intensity and sharpness of the peak appearing at $\sim 7 \text{ \AA}$ (*001*) in AMO are even lower as compared to that in OL-1. The peak at 3.57 \AA (*002*) in OL-1 is weak in AMO. This trend indicates that the number of sheets stacked per particle is smaller in AMO than in OL-1.^{43,50} The X-ray pattern of OMS-2 shows a cryptomelane type tunnel structure. The XRD peaks of the OMS-2 sample are broad indicating smaller crystallite sizes.²⁷

In manganese oxides, the Raman band occurring above 600 cm^{-1} is characteristic of the Mn–O symmetric stretching vibrational mode perpendicular to the chains of MnO₆ octahedra.⁴⁴ This band is observed at 637 cm^{-1} in OL-1, shifts to 650 cm^{-1} in OMS-2, and further shifts to 657 cm^{-1} in AMO (Figure 4). The observed shift of this band to higher wavenumbers correlates to lower number of edges shared per MnO₆ octahedron and decreased lattice distortion.⁴⁴ Birnessite (OL-1) has a 2-dimensional open layered structure and shares 4.8 edges per MnO₆ octahedron.⁵¹ On the other hand, a tunnel structure like cryptomelane (OMS-2) shares 4 edges per MnO₆ octahedron.⁵¹ In AMO, the further shift to 657 cm^{-1} indicates less than 4 edges shared per MnO₆ octahedron.^{44,51} This shift also indicates a weak interaction between adjacent MnO₂ sheets.⁴⁴

The Raman band appearing around 570 cm^{-1} is a stretching vibration of the Mn–O bond along the chains of MnO₆ octahedra. In OL-1, this band is very prominent due to the open framework of edge sharing MnO₆ octahedra.⁵¹ This band also occurs in tunnel structure OMS-2 at 578 cm^{-1} with low intensity (Figure 4). However, in AMO this band is not seen, hence AMO does not contain well formed extended MnO₆ octahedral chains, in contrast to those seen in birnessite OL-1 or OMS-2.

Infrared characterization of AMO shows two broad features (519 and 437 cm^{-1}) suggesting that AMO is still a structural variant of naturally occurring birnessite. Such a structure has also been described as vernadite (Figure 5).⁵² The structure contains a highly disordered, poorly crystalline, random packing of MnO₂ sheets up to a few layers.⁴⁶ The broadness and poor resolution of the bands in AMO (519 cm^{-1} and 437 cm^{-1}) clearly indicate a high disorder in the structure unlike in OL-1 (484 cm^{-1} and 516 cm^{-1}) (Figure 5).⁴⁶

Composition of Catalysts. Even though XRD and FTIR data show that both AMO and OL-1 belong to the birnessite family, synthesis conditions employed to generate OL-1 and AMO helps explain the compositional differences between them and this relates to their catalytic performances. The sheets of birnessite are comprised of edge sharing MnO₆ octahedra and carry a negative charge. There are two reasons for charge imbalance in birnessite sheets: (1) presence of Mn³⁺ ions in the sheets and (2) cation vacancies generated by the absence of Mn⁴⁺ ions in their octahedral sites thus creating a tetravalent negative charge at each site.⁵⁰

OL-1 was prepared under highly alkaline conditions (pH > 12). Under these preparative conditions, birnessite that forms has a triclinic unit cell and contains (MnO₂)^{x-} sheets in which all octahedral sites are filled with Mn atoms. Charge imbalance in the MnO₂ sheets is due to Mn³⁺ ions. This is supported by the AOS of Mn in OL-1 being 3.63, a high potassium content (14%) as detected by ICP-AES, and a K/Mn ratio of 0.18 as detected by EDX spectroscopy (Table 1).⁵⁰ K⁺ ions in the interlayer balance charge.

By changing the synthesis pH to acidic conditions, the triclinic unit cell of birnessite transforms into a hexagonal unit cell. Hexagonal birnessites contain octahedral cation vacancies due to missing Mn⁴⁺ ions in the (MnO₂)^{x-} sheets. During the transformation from triclinic to hexagonal unit cell, Mn³⁺ ions in the sheets of triclinic birnessite disproportionate into Mn⁴⁺ and Mn²⁺. Therefore, hexagonal birnessites contain a lower percentage of Mn³⁺ than triclinic birnessite. Hexagonal birnessites are highly disordered, poorly crystalline, and have a Mn oxidation state close to 4.0.⁵⁰ A tetravalent negative charge is created at every cation vacancy. Structural charge in the sheets is compensated by triple corner sharing Mn³⁺ octahedra in the interlayer, hydrated interlayer cations (K⁺) and protons.²²

This is the case in AMO, where the synthesis was carried out at pH 6–7 with oxalic acid. The AOS of Mn equals 3.91 in AMO (which is close to acid birnessite, δ -MnO₂, or biogenic manganese oxide) and the sample has very low potassium content (2%) compared to OL-1 (14%). EDX analysis shows a surface K/Mn ratio of 0.01. The structure of AMO is analogous to hexagonal birnessites such as H⁺-birnessite,^{21,50} biogenic layered MnO₂,²² or δ -MnO₂. A figure depicting a well formed triclinic birnessite sheet containing a well-ordered large proportion of Mn³⁺ in the sheets is shown in contrast to the poorly crystalline hexagonal birnessite sheet with vacant octahedral sites (Figure 12).⁵⁰ The Mn³⁺ species in triclinic birnessites are located in the (MnO₂)^{x-} layers. A row of Mn³⁺ species alternates with two rows of Mn⁴⁺ in the layers. In hexagonal birnessites, the Mn³⁺ species are located in interlayers above vacant sites.⁵³

The BET surface area of AMO ($184 \text{ m}^2/\text{g}$) and nanoparticles of <10 nm sizes bears similarities to biogenic manganese oxides.^{21,22,50} Raman data further indicate low polymerization of the MnO₂ sheets, and hence the absence of extended MnO₆

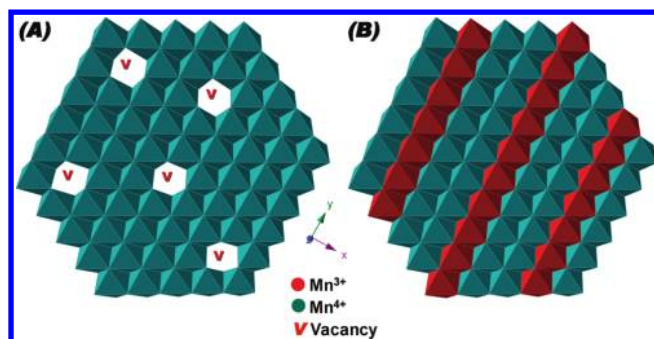


Figure 12. (A) Single sheet of hexagonal birnessite vs (B) single sheet of triclinic birnessite. (Figure adapted from reference 50).

networks. IR analysis shows that the structure is similar to vernadite (δ - MnO_2).

Comparison with Other Manganese Oxide Catalysts from Literature. Manganese oxide catalysts reported in the literature were also investigated (Figure 11). The BET surface area of KIT-6/Mn (495 m^2/g) was much higher than that of AMO (184 m^2/g) or α - MnO_2 nanotubes (75 m^2/g) (Table 3).

Table 3. Turnover Numbers for Manganese Catalysts and BET Surface Areas of Catalysts (All Catalysts Were Tested with CAN Oxidant)

catalyst	ref no.	TON (mmol O_2 /mol Mn)	BET surface area ^a (m^2/g)
AMO	this work	242	184
α - MnO_2 -nanotubes	48	211	75
λ - MnO_2 -LT	47	112	42
CaMn_2O_4	16	67	13
KIT-6/Mn-clusters	17	41	495
MnO_2	18	33	21

^aMeasured BET surface area.

However, AMO and α - MnO_2 nanotubes gave higher turnover numbers (Table 3). Second, in the case of the MnO_2 catalyst¹⁸ XRD data showed no peaks suggesting that this catalyst has an amorphous structure; however its catalytic activity was much lower than that of AMO or crystalline α - MnO_2 nanotubes.

Catalytic Activity. The high catalytic activity of AMO is related to its structure, which is a layered manganese oxide analogous to hexagonal birnessite with cation vacancies in the MnO_2 sheet as described in the previous section.^{32,54} Cation vacancies in AMO are influential in catalytic activity due to coordinatively unsaturated oxygens that are excellent sites for proton binding. The μ -OH units thus created at vacancy or edge sites can undergo deprotonation and help in proton coupled electron transfer during water oxidation catalysis.⁵⁵ In addition, smaller particle sizes (less than 10 nm) and high surface area results in larger number of edge sites that is available for water molecules to bind. Consequently, the surface of AMO presents more sites for the coordination of water molecules to the catalyst surface.^{22,55} In contrast, such conditions are unavailable on a perfectly filled $\text{Mn}^{3+}/\text{Mn}^{4+}$ birnessite (OL-1) MnO_2 sheet (Figure 12), and this relates to the poor catalytic performance of OL-1.

OMS-2 is a 2×2 tunnel structure with nanorod lengths going up to approximately 100 nm. In the case of tunnel structures only edges of the tunnels may provide reactive

sites.⁴⁷ Mn_4O_4 configurations that can form on the edges of the tunnels of OMS-2 might lead to high activity. The Mn–Mn vectors in OMS-2 type tunnel molecules, gives rise to a variety of Mn_4O_4 geometric arrangements some of which may be similar to the OEC complex in PS-II.³¹

CONCLUSIONS

In conclusion, manganese oxide layered and tunnel structures were studied as water oxidation catalysts. Amorphous manganese oxides (AMO) were found to be highly active compared to cryptomelane-type tunnel manganese oxides (OMS-2) or layered birnessite (OL-1) under chemical and photochemical water oxidation conditions. AMO catalyst could be regenerated after reaction. High turnover numbers were obtained with AMO compared to several other manganese oxides. GC studies showed oxygen evolution for extended time periods. AMO is a disordered mixed valent ($\text{Mn}^{4+}/\text{Mn}^{3+}$) manganese oxide consisting of nanoparticles of less than 10 nm sizes, a high surface area (184 m^2/g), and an average oxidation state of Mn = 3.91. TEM images show randomly oriented crystallites, and XRD shows a layered material resembling turbostratic birnessite. However, major structural and compositional differences are determined by Raman and FTIR spectroscopy and compositional analysis.

The characterization data suggest that AMO is similar to H^+ -birnessite or layered biogenic manganese oxides that contain cation vacancies in the structure with hexagonal unit cells. Raman data show low polymerization of the MnO_2 sheets. These factors are influential in catalytic activity. Hence, amorphous manganese oxides are potential candidates for commercial water splitting. This study provides insight for future investigations of layered and tunnel Mn-oxide water splitting catalysts due to their ubiquity in nature.

ASSOCIATED CONTENT

Supporting Information

TGA graphs of AMO, OL-1, and OMS-2 catalysts, mass spectrometric detection of gas products from water oxidation reactions using ^{18}O -labeled and unlabeled water with AMO catalyst, infrared spectra of AMO catalyst before and after reaction, XRD patterns of catalysts after reaction, EDX analysis of spent AMO catalyst after reaction, and AAS analysis for detection of Mn in reactant solutions. This material is available free of charge via the Internet at <http://pubs.acs.org>.

AUTHOR INFORMATION

Corresponding Author

*Phone: (614)-292-4532 (P.K.D.); (860)-486-2797 (S.L.S.). Fax: (614)-292-1685 (P.K.D.); (860)-486-2981 (S.L.S.). E-mail: dutta@chemistry.ohio-state.edu (P.K.D.); steven.suib@uconn.edu (S.L.S.).

Notes

The authors declare no competing financial interest.

ACKNOWLEDGMENTS

We acknowledge support from the Chemical Sciences, Geosciences and Biosciences division, Office of Basic Energy Sciences, Office of Science, and U.S. Department of Energy for funding (DE-FG02-86ER13622.A000). The authors would like to thank Dr. Francis Galasso for helpful discussions and Justin Reutenaur for help with thermogravimetric analysis.

REFERENCES

- (1) U.S. Energy Information Administration, Annual Energy Outlook 2011. [http://www.eia.gov/forecasts/aeo/pdf/0383\(2011\).pdf](http://www.eia.gov/forecasts/aeo/pdf/0383(2011).pdf) (accessed November/2, 2011).
- (2) U.S. Energy Information Administration, Annual Energy Review 2010. <http://www.eia.gov/totalenergy/data/annual/pdf/aer.pdf> (accessed November/2, 2011).
- (3) Lewis, N. S.; Nocera, D. G. *Proc. Natl. Acad. Sci. U. S. A.* **2006**, *103*, 15729–15735.
- (4) U.S. Energy Information Administration, U.S. Energy-Related Carbon Dioxide Emissions. <http://www.eia.gov/environment/emissions/carbon/> (accessed November/2, 2011).
- (5) Turner, J. *Nat. Mater.* **2008**, *7*, 770–771.
- (6) Eisenberg, R. *Science* **2009**, *324*, 44–45.
- (7) Jiao, F.; Frei, H. *Angew. Chem., Int. Ed. Engl.* **2009**, *48*, 1841–1844.
- (8) Kanan, M. W.; Nocera, D. G. *Science* **2008**, *321*, 1072–1075.
- (9) Harriman, A.; Pickering, I. J.; Thomas, J. M.; Christensen, P. A. *J. Chem. Soc., Faraday Trans. 1* **1988**, *84*, 2795–2806.
- (10) Das, S. K.; Dutta, P. K. *Microporous Mesoporous Mater.* **1998**, *22*, 475–483.
- (11) Hara, M.; Waraksa, C. C.; Lean, J. T.; Lewis, B. A.; Mallouk, T. E. *J. Phys. Chem. A* **2000**, *104*, 5275–5280.
- (12) Hull, J. F.; Balcells, D.; Blakemore, J. D.; Incarvito, C. D.; Eisenstein, O.; Brudvig, G. W.; Crabtree, R. H. *J. Am. Chem. Soc.* **2009**, *131*, 8730–8731.
- (13) Xu, Y.; Aakermark, T.; Gyollai, V.; Zou, D.; Eriksson, L.; Duan, L.; Zhang, R.; Aakermark, B.; Sun, L. *Inorg. Chem.* **2009**, *48*, 2717–2719.
- (14) Allen, J. F.; Martin, W. *Nature* **2007**, *445*, 610–612.
- (15) Dismukes, G. C.; Brimblecombe, R.; Felton, G. A. N.; Pryadun, R. S.; Sheats, J. E.; Spiccia, L.; Swiegers, G. F. *Acc. Chem. Res.* **2009**, *42*, 1935–1943.
- (16) Najafpour, M. M.; Ehrenberg, T.; Wiechen, M.; Kurz, P. *Angew. Chem., Int. Ed.* **2010**, *49* (2233–2237), S2233/1–S2233/15.
- (17) Jiao, F.; Frei, H. *Chem. Commun.* **2010**, *46*, 2920–2922.
- (18) Shafirovich, V. Y.; Khannanov, N. K.; Shilov, A. E. *J. Inorg. Biochem.* **1981**, *15*, 113–129.
- (19) Post, J. E. *Proc. Natl. Acad. Sci. U. S. A.* **1999**, *96*, 3447–3454.
- (20) Spiro, T. G.; Bargar, J. R.; Sposito, G.; Tebo, B. M. *Acc. Chem. Res.* **2010**, *43*, 2–9.
- (21) Villalobos, M.; Lanson, B.; Manceau, A.; Toner, B.; Sposito, G. *Am. Mineral.* **2006**, *91*, 489–502.
- (22) Grangeon, S.; Lanson, B.; Miyata, N.; Tani, Y.; Manceau, A. *Am. Mineral.* **2010**, *95*, 1608–1616.
- (23) Luo, J.; Zhang, Q.; Garcia-Martinez, J.; Suib, S. L. *J. Am. Chem. Soc.* **2008**, *130*, 3198–3207.
- (24) Suib, S. L. *Acc. Chem. Res.* **2008**, *41*, 479–487.
- (25) Sithambaram, S.; Ding, Y.; Li, W.; Shen, X.; Gaenzler, F.; Suib, S. L. *Green Chem.* **2008**, *10*, 1029–1032.
- (26) Son, Y.; Makwana, V. D.; Howell, A. R.; Suib, S. L. *Angew. Chem., Int. Ed.* **2001**, *40*, 4280–4283.
- (27) Iyer, A.; Galindo, H.; Sithambaram, S.; King'ondeu, C.; Chen, C.; Suib, S. L. *Appl. Catal. A: Gen.* **2010**, *375*, 295–302.
- (28) *Handbook of Layered Materials*; Auerbach, S. M., Carrado, K. A., Dutta, P. K., Eds.; Marcel Dekker, Inc.: New York, 2004.
- (29) Suib, S. L. *J. Mater. Chem.* **2008**, *18*, 1623–1631.
- (30) Suib, S. L. *Curr. Opin. Solid State Mater. Sci.* **1998**, *3*, 63–70.
- (31) Sauer, K.; Yachandra, V. K. *Proc. Natl. Acad. Sci. U. S. A.* **2002**, *99*, 8631–8636.
- (32) Swiegers, G. F.; Clegg, J. K.; Stranger, R. *Chem. Sci.* **2011**, *2*, 2254–2262.
- (33) Messinger, J.; Robblee, J. H.; Bergmann, U.; Fernandez, C.; Glatzel, P.; Visser, H.; Cinco, R. M.; McFarlane, K. L.; Bellacchio, E.; Pizarro, S. A.; Cramer, S. P.; Sauer, K.; Klein, M. P.; Yachandra, V. K. *J. Am. Chem. Soc.* **2001**, *123*, 7804–7820.
- (34) Cao, H.; Suib, S. L. *J. Am. Chem. Soc.* **1994**, *116*, 5334–5342.
- (35) Chen, J.; Lin, J. C.; Purohit, V.; Cutlip, M. B.; Suib, S. L. *Catal. Today* **1997**, *33*, 205–214.
- (36) Genuino, H. C.; Njagi, E. C.; Benbow, E. M.; Hoag, G. E.; Collins, J. B.; Suib, S. L. *J. Photochem. Photobiol., A* **2011**, *217*, 284–292.
- (37) Segal, S. R.; Suib, S. L.; Tang, X.; Satyapal, S. *Chem. Mater.* **1999**, *11*, 1687–1695.
- (38) Chen, C.; Njagi, E. C.; Sun, S.; Genuino, H.; Hu, B.; Suib, S. L. *Chem. Mater.* **2010**, *22*, 3313–3315.
- (39) Kurz, P.; Berggren, G.; Anderlund, M. F.; Styring, S. *Dalton Trans.* **2007**, 4258–4261.
- (40) Ding, Y.; Shen, X.; Sithambaram, S.; Gomez, S.; Kumar, R.; Crisostomo, V. M. B.; Suib, S. L.; Aindow, M. *Chem. Mater.* **2005**, *17*, 5382–5389.
- (41) Gao, Q.; Giraldo, O.; Tong, W.; Suib, S. L. *Chem. Mater.* **2001**, *13*, 778–786.
- (42) Luo, J.; Zhang, Q.; Suib, S. L. *Inorg. Chem.* **2000**, *39*, 741–747.
- (43) Polzer, F.; Kunz, D. A.; Breu, J.; Ballauff, M. *Chem. Mater.* **2010**, *22*, 2916–2922.
- (44) Julien, C.; Massot, M.; Baddour-Hadjean, R.; Franger, S.; Bach, S.; Pereira-Ramos, J. P. *Solid State Ionics* **2003**, *159*, 345–356.
- (45) Kingondu, C. K.; Opembe, N.; Chen, C.; Ngala, K.; Huang, H.; Iyer, A.; Garces, H. F.; Suib, S. L. *Adv. Funct. Mater.* **2011**, *21*, 312–323.
- (46) Potter, R. M.; Rossman, G. R. *Am. Mineral.* **1979**, *64*, 1199–1218.
- (47) Robinson, D. M.; Go, Y. B.; Greenblatt, M.; Dismukes, G. C. *J. Am. Chem. Soc.* **2010**, *132*, 11467–11469.
- (48) Boppana, V. B. R.; Jiao, F. *Chem. Commun.* **2011**, *47*, 8973–8975.
- (49) Drits, V. A.; Silvester, E.; Gorshkov, A. I.; Manceau, A. *Am. Mineral.* **1997**, *82*, 946–961.
- (50) Villalobos, M.; Toner, B.; Bargar, J.; Sposito, G. *Geochim. Cosmochim. Acta* **2003**, *67*, 2649–2662.
- (51) Julien, C. M.; Massot, M.; Poinsignon, C. *Spectrochim. Acta, Part A* **2004**, *60A*, 689–700.
- (52) Chukhrov, F. V.; Gorshkov, A. I.; Rudnitskaya, E. S.; Berezovskaya, V. V.; Sivtsov, A. V. *Clays Clay Miner.* **1980**, *28*, 346–354.
- (53) Gaillot, A.; Flot, D.; Drits, V. A.; Manceau, A.; Burghammer, M.; Lanson, B. *Chem. Mater.* **2003**, *15*, 4666–4678.
- (54) Hocking, R. K.; Brimblecombe, R.; Chang, L.; Singh, A.; Cheah, M. H.; Glover, C.; Casey, W. H.; Spiccia, L. *Nat. Chem.* **2011**, *3*, 461–466.
- (55) Zaharieva, I.; Najafpour, M. M.; Wiechen, M.; Haumann, M.; Kurz, P.; Dau, H. *Energy Environ. Sci.* **2011**, *4*, 2400–2408.